

Supplementary Materials for

Zero-strain $K_{0.6}Mn_1F_{2.7}$ hollow nanocubes for ultrastable potassium ion storage

Zhiwei Liu,^{a†} Ping Li,^{a†} Guoquan Suo,^a Sheng Gong,^b Wei Wang,^{*bc} Cheng-Yen Lao,^c Yajie Xie,^a Hao Guo,^d Qiya Yu,^a Wang Zhao,^a Kun Han,^a Qian Wang,^b Mingli Qin,^a Kai Xi,^c Xuanhui Qu^{*a}

^a Institute for Advanced Materials and Technology, University of Science and Technology Beijing, Beijing 100083, China.

^b Department of Materials Science and Engineering, College of Engineering, Peking University, Beijing 100871, China.

^c Department of Materials Science and Metallurgy, University of Cambridge, Cambridge, CB3 0FS, UK.

^d China Institute of Atomic Energy, P. O. Box 275(10), Beijing 102413, China.

†These authors contributed equally to this work.

Corresponding authors: wwangbj@pku.edu.cn; quxh@ustb.edu.cn

Supplementary Figures and Discussions

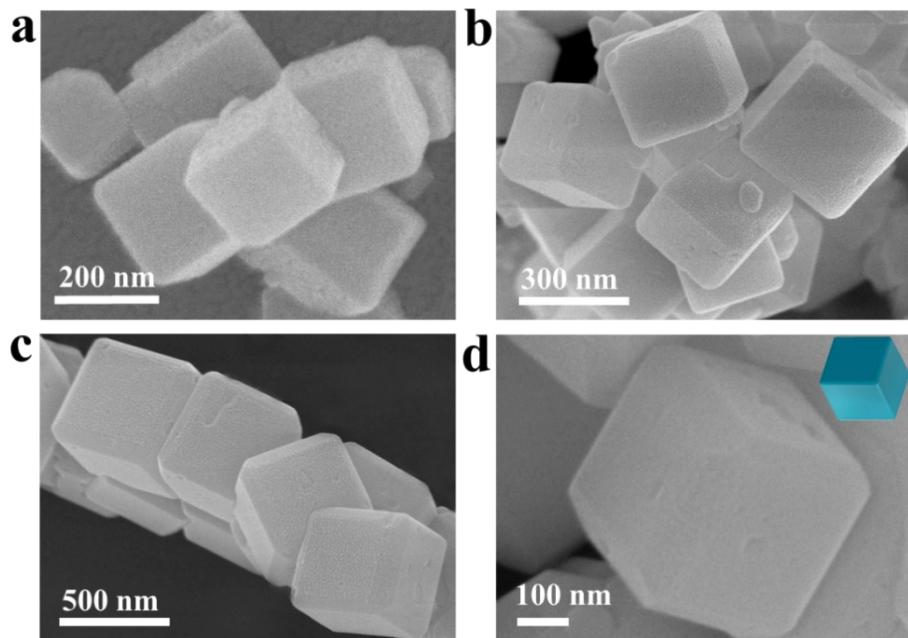


Fig. S1. FESEM images of (a) KMnF-S1, (b) KMnF-S2, (c) and (d) KMnF-L.

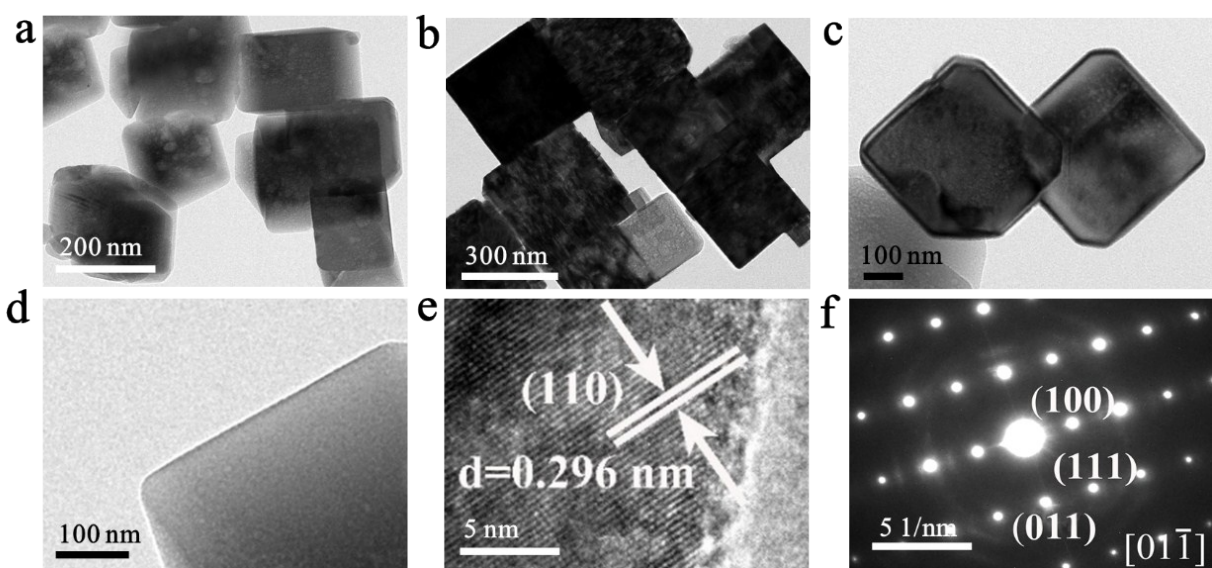


Fig. S2. TEM images of (a) KMnF-S1, (b) KMnF-S2, (c, d) KMnF-L, (e) HRTEM images and (g) SAED pattern of KMnF-L.

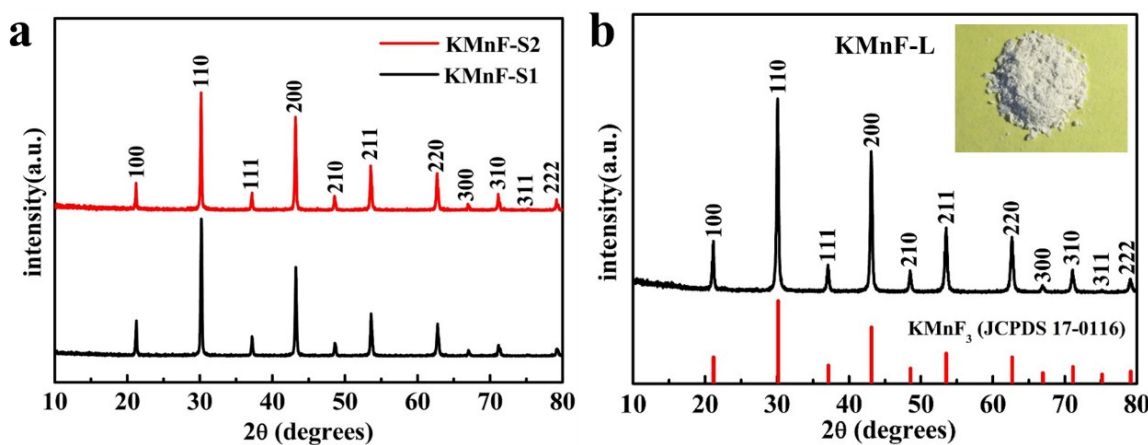


Fig. S3. The XRD patterns of (a) KMnF-S1 and KMnF-S2, (b) KMnF-L (inset: digital photo).

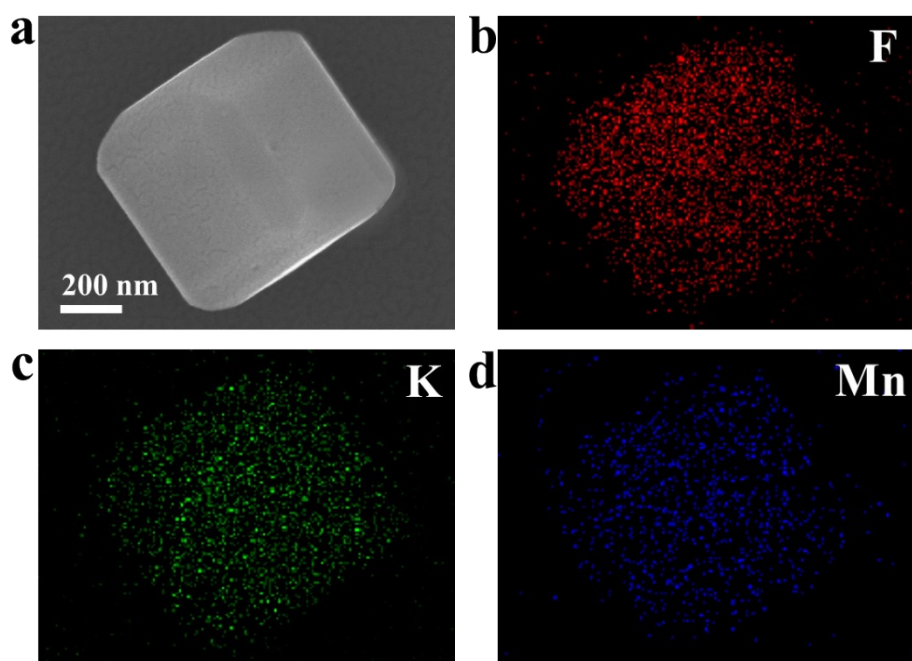


Fig. S4. FESEM mapping of KMnF-L.

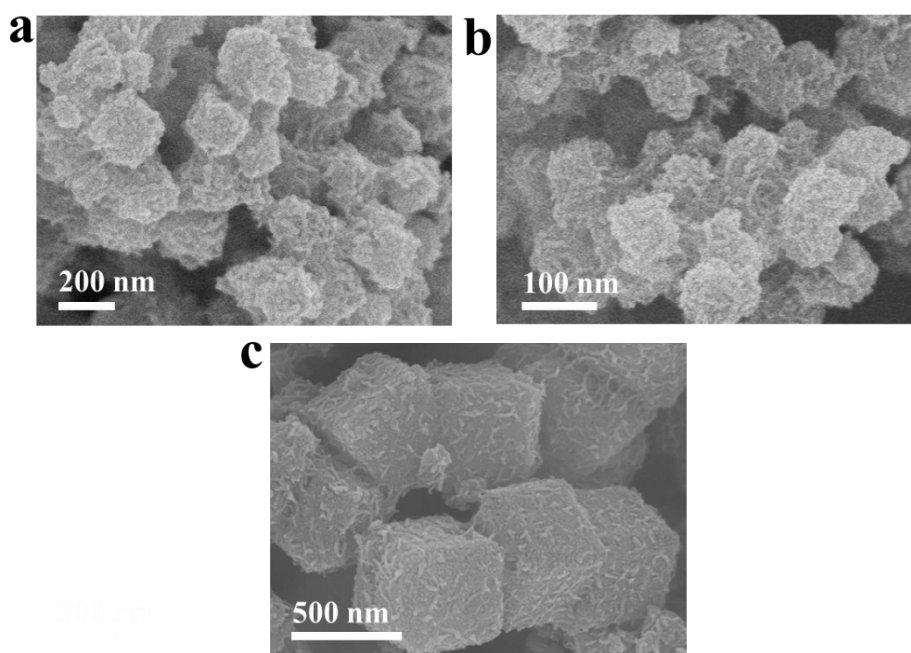


Fig. S5. FESEM images of (a) KMnF-S1E, (b) KMnF-S2E, and (c) KMnF-LE.

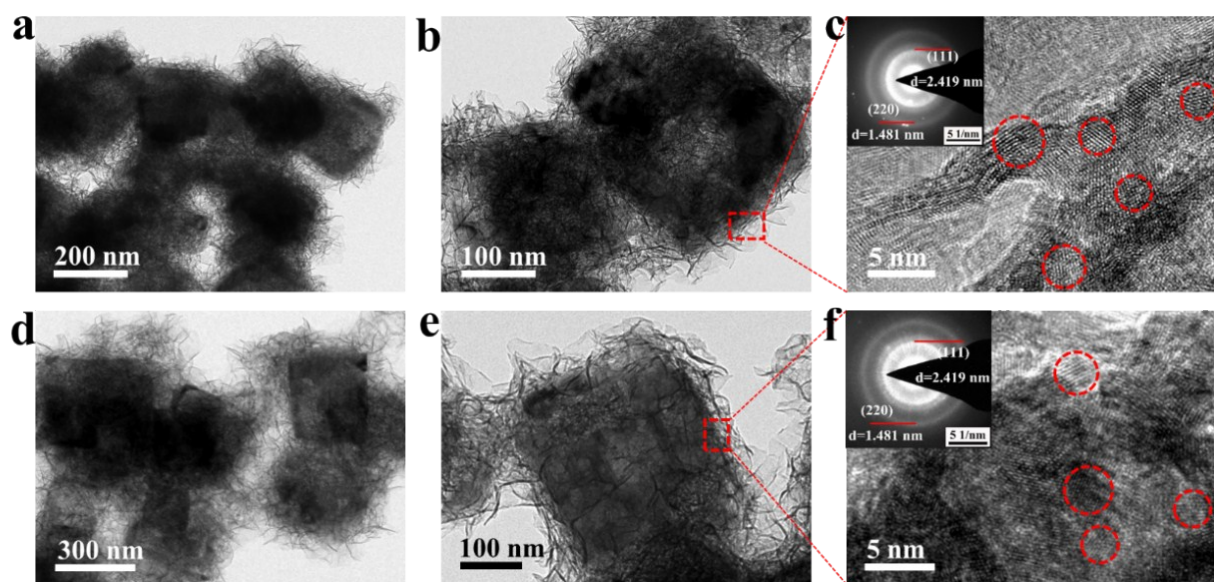


Fig. S6. TEM images of KMnF-S1E and KMnF-S2E. (a, b) TEM images, (c) HRTEM and SEAD images of KMnF-S1E, (d, e) TEM images, (f) HRTEM and SEAD images of KMnF-S2E, the red dotted lines represent different lattice plane.

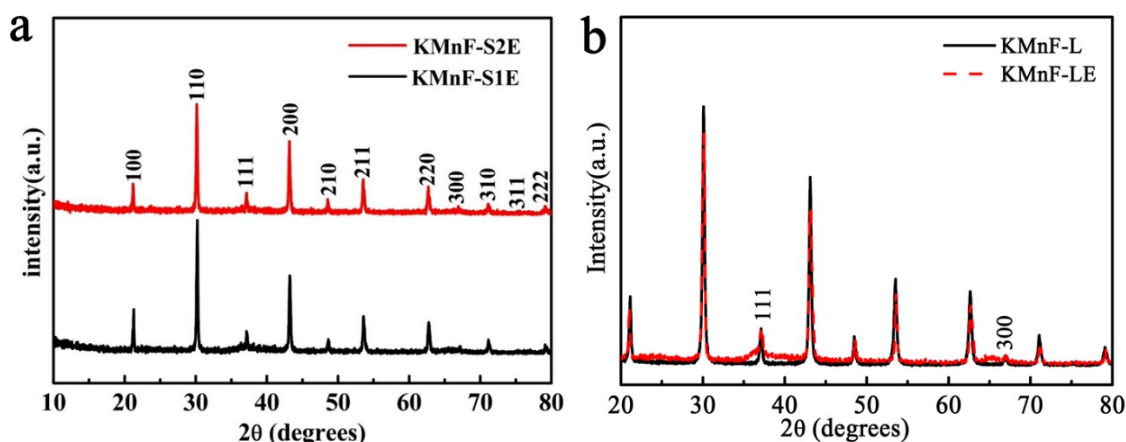


Fig. S7. (a) The XRD patterns of KMnF-S1E and KMnF-S2E, (b) The direct comparison of XRD patterns of KMnF-LE and KMnF-L.

As shown in Fig. S7b, the powder XRD pattern of KMnF-LE shows more broadening peaks at the positions of (111) and (300) crystal planes. We measured the half-peak width of the (111) crystal plane of KMnF-LE and KMnF-L, the half-peak width of (111) crystal plane of KMnF-LE is 0.76° , while that of KMnF-L is 0.42° . Therefore, it can be seen that the degree of crystallization decreases after etching.

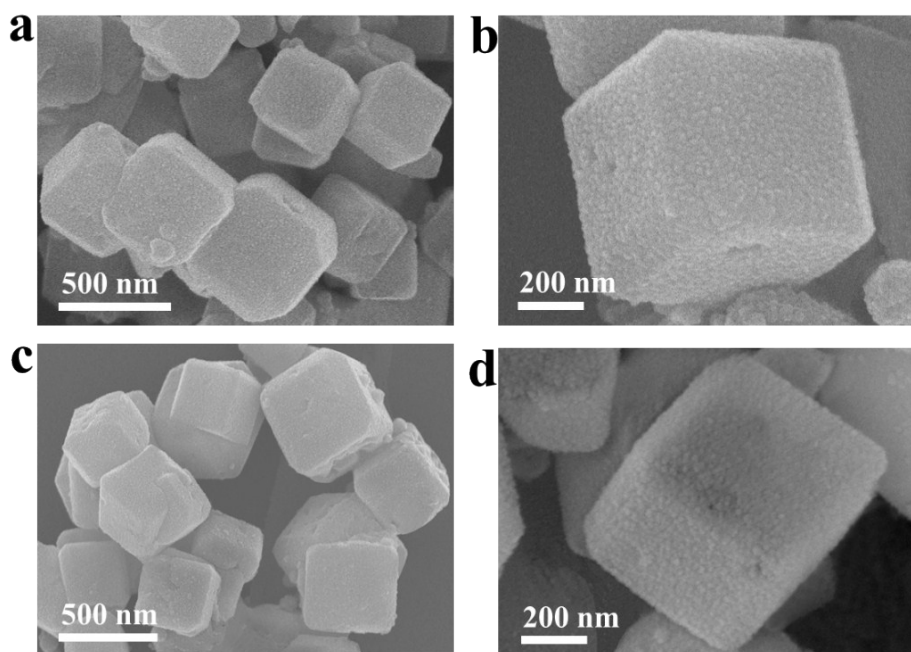


Fig. S8. Investigation of time-dependent evolution of interior hollow cavity characterized by FESEM for KMnF-LE. The applied etching times were (a, b) 0.25 h and (c, d) 1 h.

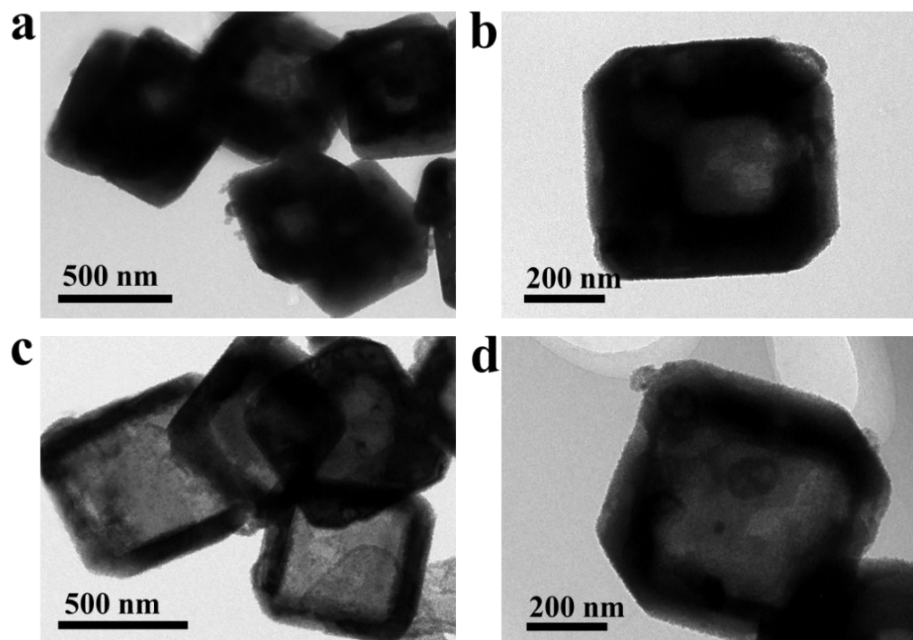


Fig. S9. Investigation of time-dependent evolution of interior hollow cavity characterized by TEM for KMnF-LE. The applied etching times were (a, b) 0.25 h and (c, d) 1 h.

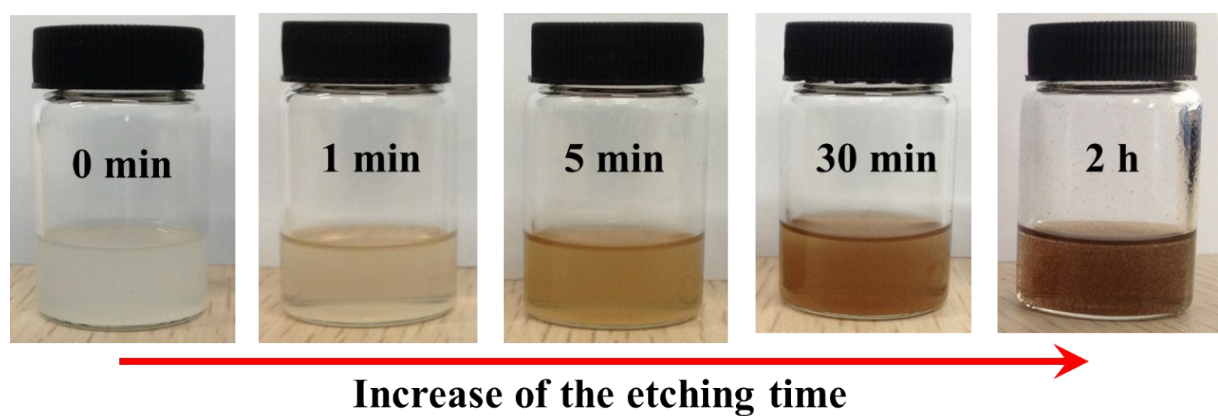


Fig. S10. Photograph of the etching process of KMnF-LE with different the etching time.

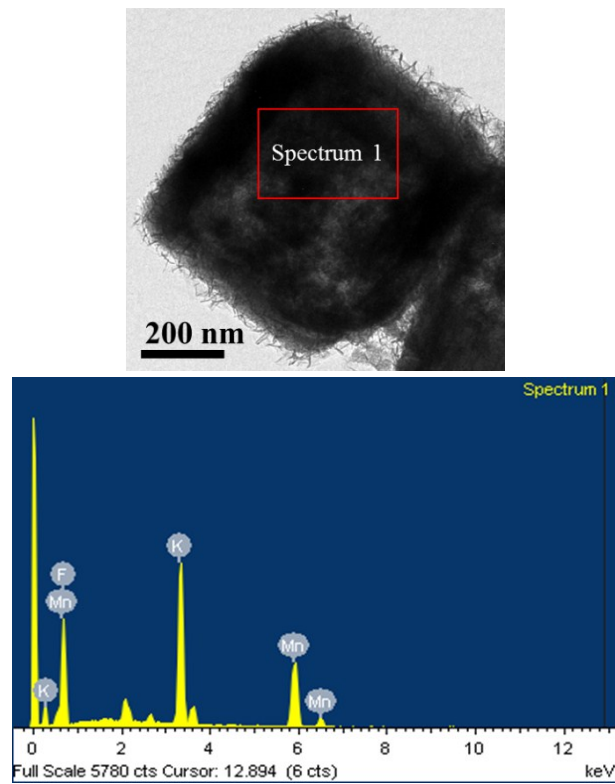


Fig. S11. TEM micrographs and EDS spectra of KMnF-LE. Elemental spectra corresponds to the Spectrum 1 point on the TEM micrograph.

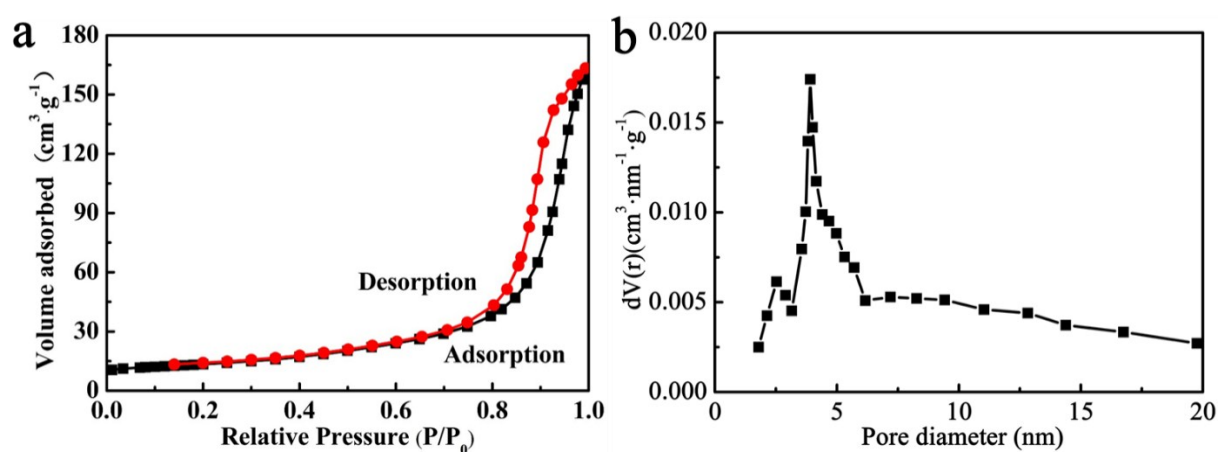


Fig. S12. (a) Nitrogen adsorption-desorption isotherms and (b) Pore-size distribution of as-prepared KMnF-L.

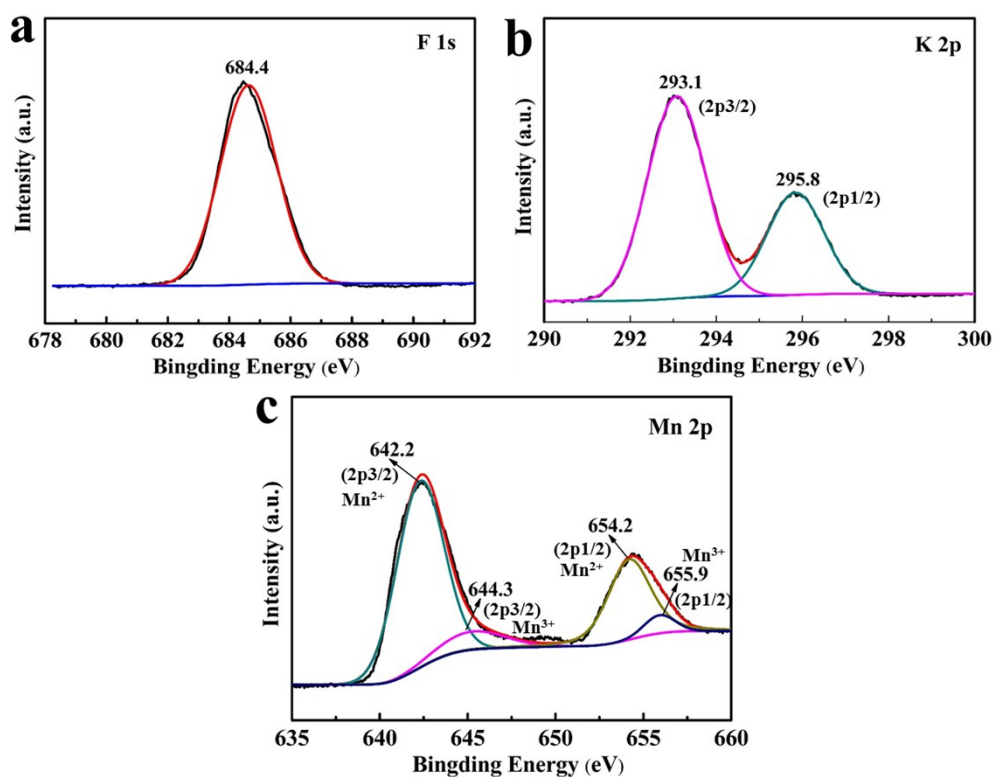


Fig. S13. XPS spectra of as-prepared KMnF-L: (a) F 1s, (b) K 2p, (c) Mn 2p peaks.

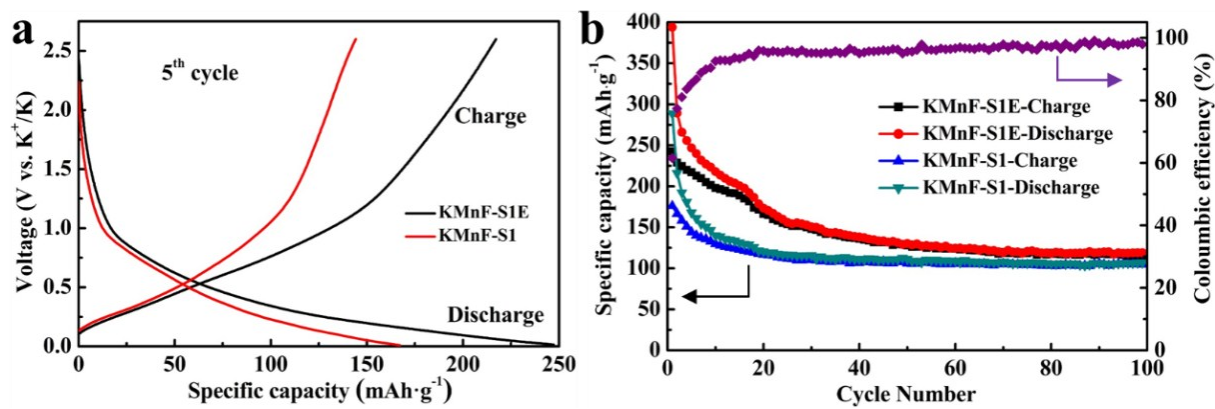


Fig. S14. (a) Discharge/charge voltage profiles of KMnF-S1 and KMnF-S1E with the 5th cycling, (b) Cycling performance of KMnF-S1 and KMnF-S1E at a current rate of 50 mA g⁻¹.

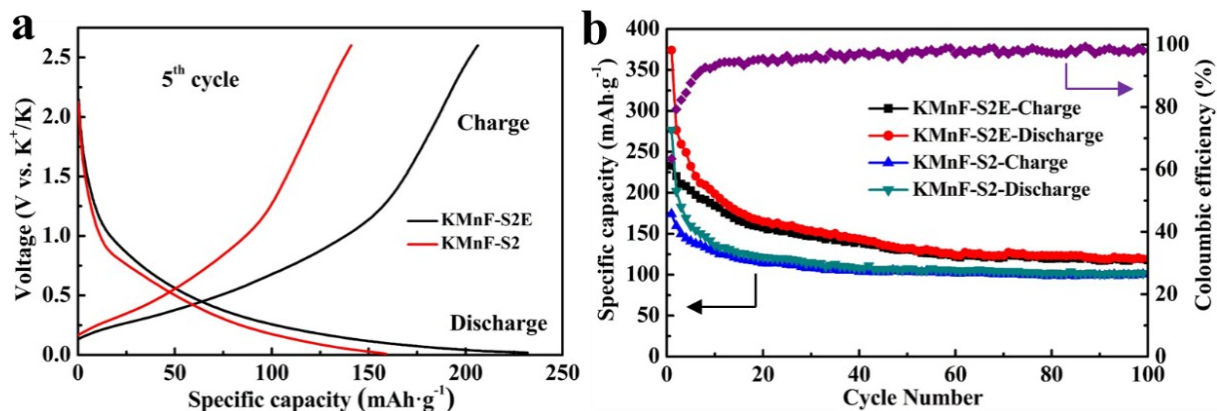


Fig. S15. (a) Discharge/charge voltage profiles of KMnF-S2 and KMnF-S2E with the 5th cycling, (b) Cycling performance of KMnF-S2 and KMnF-S2E at a current rate of 50 mA g⁻¹.

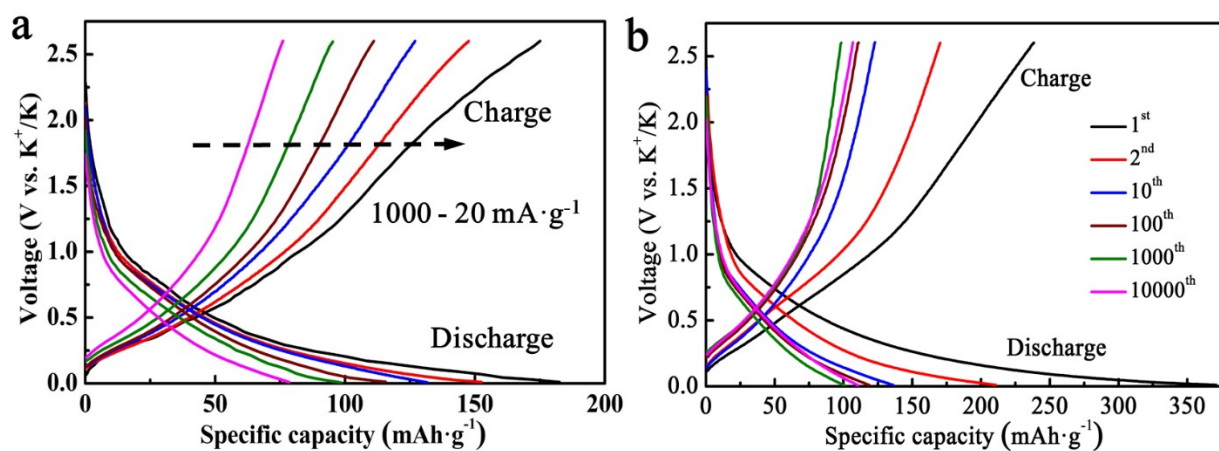


Fig. S16. (a) Galvanostatic discharge/charge curves of KMnF-LE/K battery at different rates. From right to left: 20, 50, 100, 200, 500 and 1000 $\text{mA} \cdot \text{g}^{-1}$, (b) The 1st, 2nd, 10th, 100th, 1000th and 10000th charge/discharge curves of KMnF-LE at 400 $\text{mA} \cdot \text{g}^{-1}$.

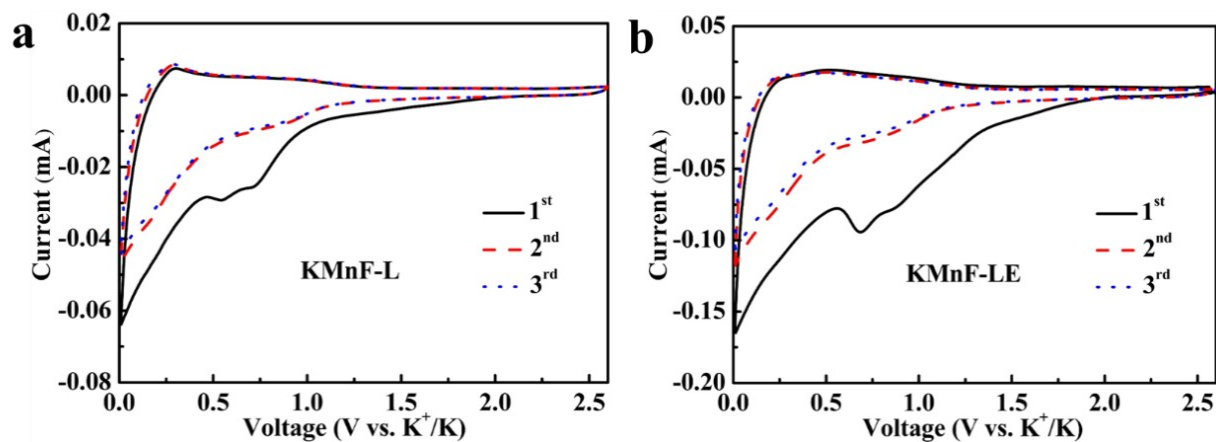


Fig. S17. Cyclic voltammograms of (a) KMnF-L and (b) KMnF-LE in the voltage range of 0.01–2.6 V at scan rates of 0.1 mV·s⁻¹.

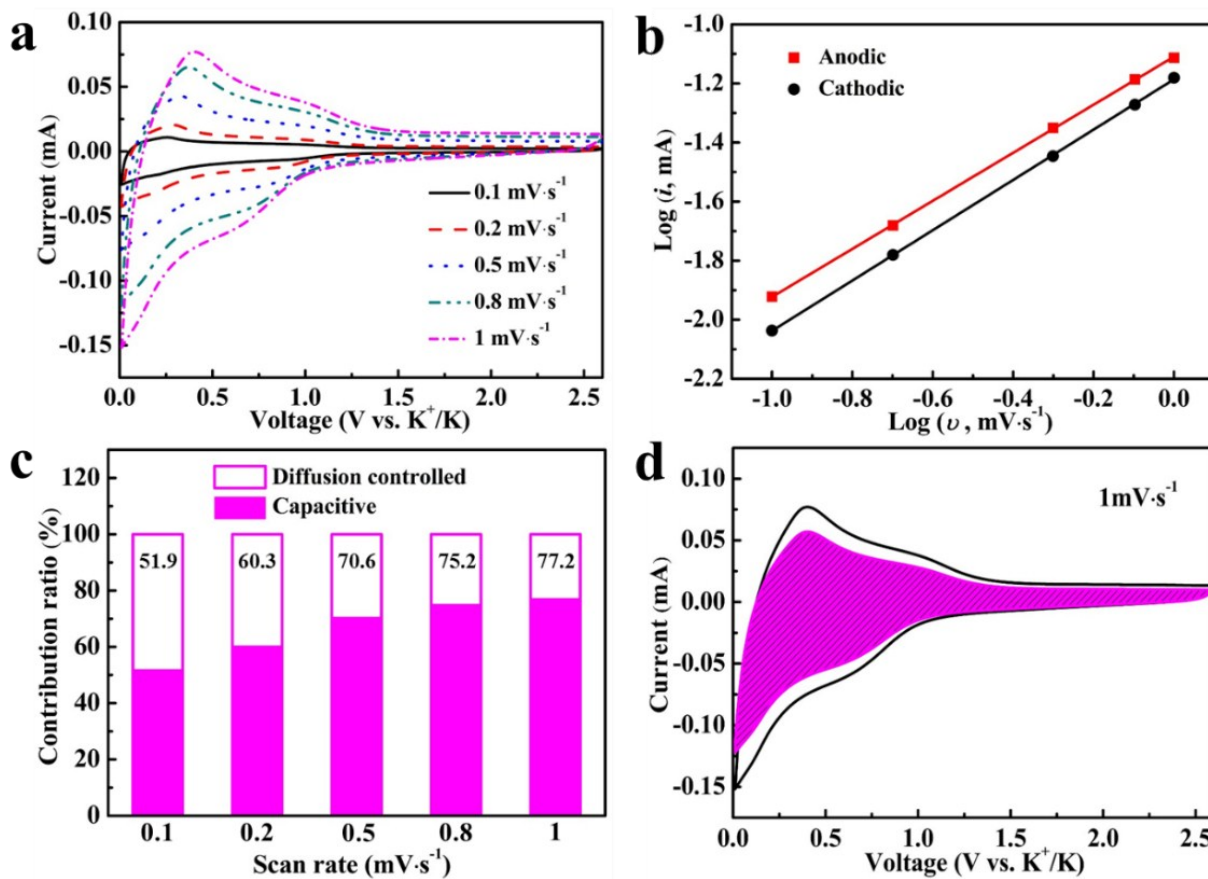


Fig. S18. The potential pseudocapacitive behavior of KMnF-L electrode. (a) CV profiles at different scan rates and (b) the plots of $\log(i)$ vs. $\log(v)$ (peak current: i , scan rate: v) of KMnF-L, (c) The percentages of pseudocapacitive contributions at different scan rates. (d) The purple region shows the CV profile with the pseudocapacitive contribution at scan rate of $1 \text{ mV}\cdot\text{s}^{-1}$.

According to the previous reports,¹ the peak current (i) and the scan rate (v) can follow the relationship of $i = av^b$. Meanwhile, the b-value can be obtained by the slope of the $\log(i)$ vs. $\log(v)$ plot. If b-value is close to 0.5, the charge storage is dominated by the ionic diffusion,² whereas the b-value of 1 represents a capacitive response.³ According to the CV profiles, there is no double-layer capacitive response, so the capacitive response is mainly pseudocapacitance.^{4,5} The b-value of 0.82 and 0.66 for KMnF-L (Fig. S18b) and KMnF-LE electrode (Fig. S19b), respectively, suggest that the charge storage behavior is controlled by both the K ion diffusion and the pseudocapacitive effect. The specific percentages of pseudocapacitive contributions at different scan rates are shown in Fig. S18c and Fig. S19c. Furthermore, the pseudocapacitive contributions at various scan rates are quantified through the Equation of $i = k_1v + k_2v^{1/2}$, where k_1v and $k_2v^{1/2}$ represent the contribution of pseudocapacitance and ionic diffusion, respectively. As the scanning rate increases, the capacitive charge contributions of KMnF-L and KMnF-LE negative electrodes will rise and finally reach the maximum values of 77.2% (Fig. S18d) and 65.2% (Fig. S19d) at $1 \text{ mV}\cdot\text{s}^{-1}$, respectively.

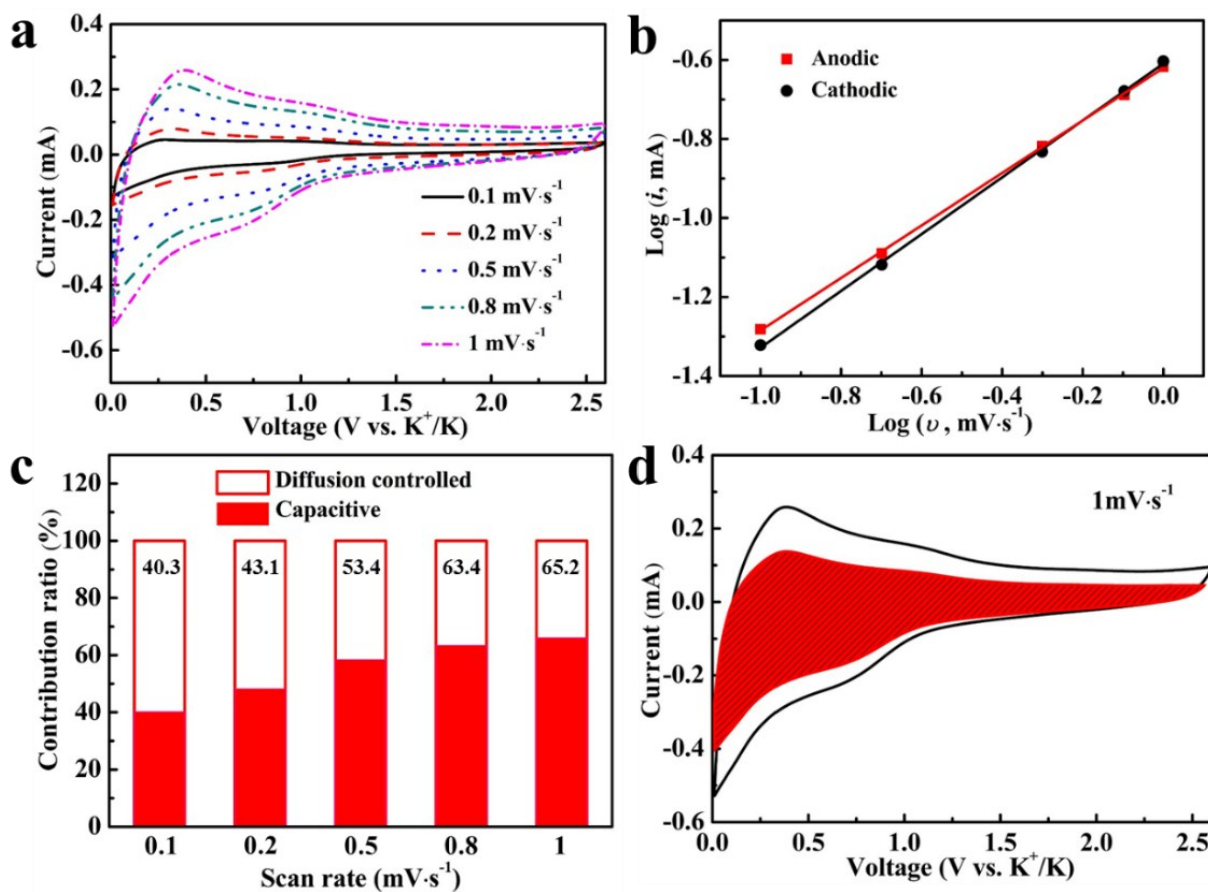


Fig. S19. The potential pseudocapacitive behavior of KMnF-LE electrode. (a) CV profiles at different scan rates and (b) the plots of $\log(i)$ vs. $\log(v)$ (peak current: i , scan rate: v) of KMnF-LE, (c) The percentages of pseudocapacitive contributions at different scan rates, (d) The red region shows the CV profile with the pseudocapacitive contribution at scan rate of $1 \text{ mV}\cdot\text{s}^{-1}$.

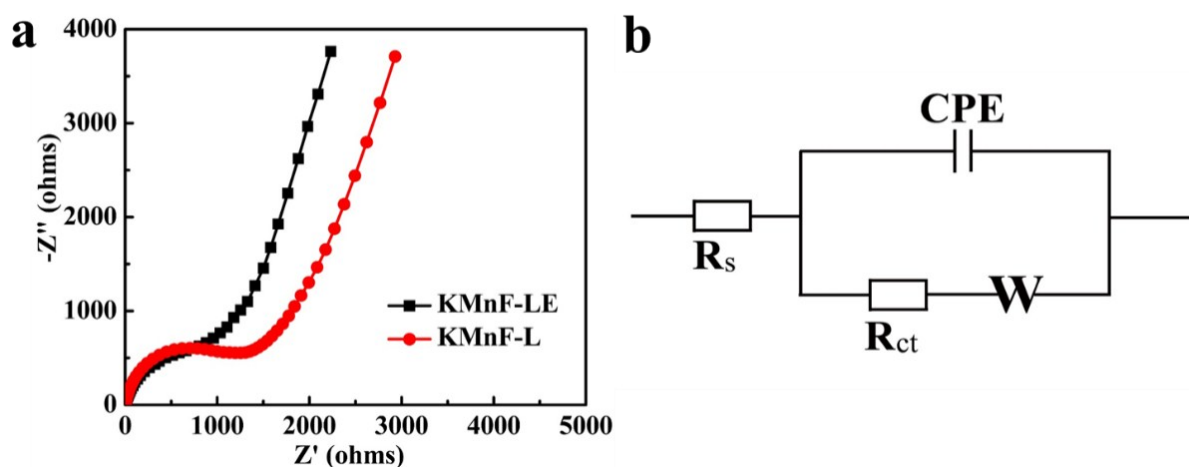


Fig. S20. (a) Nyquist plots for KMnF-L and KMnF-LE in original cycles, (b) The simplified equivalent circuit model.

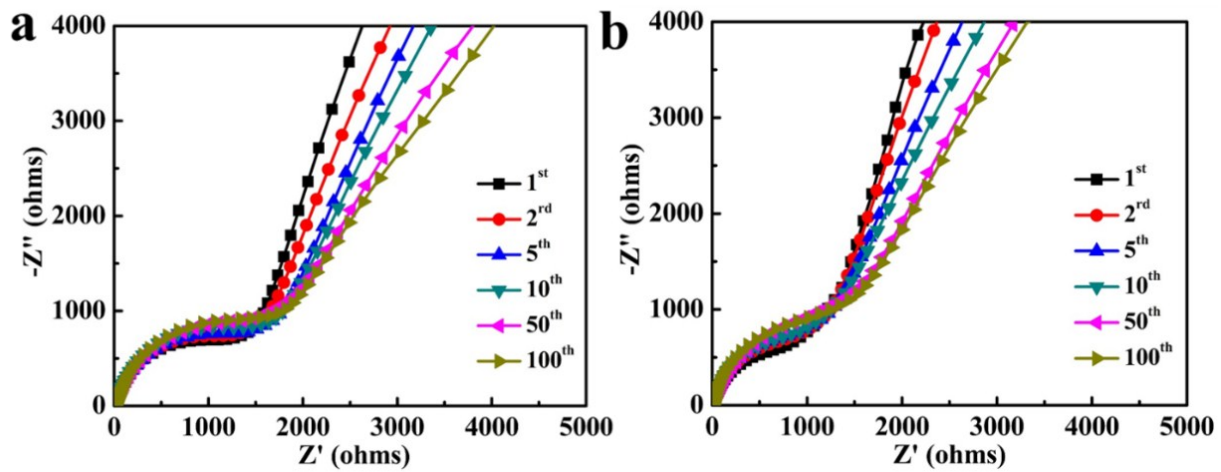


Fig. S21. Nyquist plots for (a) KMnF-L and (b) KMnF-LE in the 1st, 2nd, 5th, 10th, 50th and 100th cycling cycles.

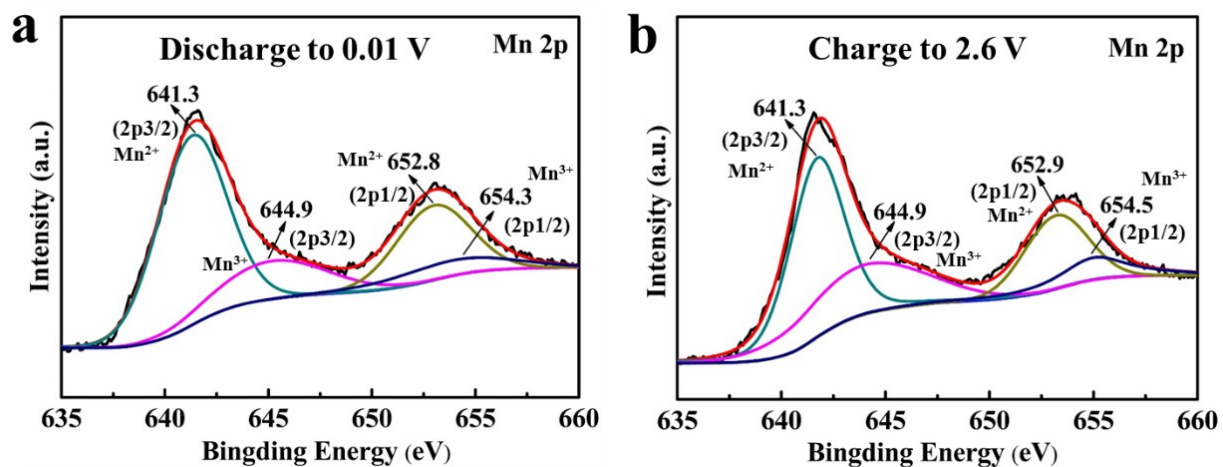


Fig. S22. XPS spectra of the cycled KMnF-LE in the Mn region. (a) Discharge to 0.01 V, (b) Charge to 2.6 V.

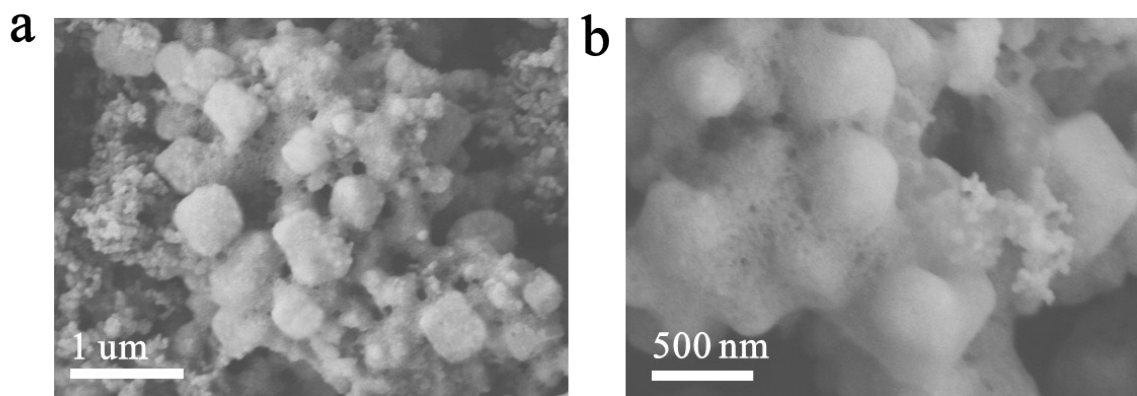


Fig. S23. FESEM images of the KMnF-LE electrode after 100 cycles at a current density of 100 mA g⁻¹.

Energy & Environmental Science

Table S1. The element content of KMnF-LE via EDS analysis.

Element	Weight %	Atomic %
F	37.02	60.17
K	19.39	15.36
Mn	43.59	24.47
Totals	100.00	100.00

Table S2. The ICP data of KMnF-L and KMnF-LE.

Element	KMnF-L	KMnF-LE
K%	23.37	18.05
Mn%	37.81	42.15

Table S3. Electrochemical performance comparison of some reported negative materials of KIBs.

Active materials	Electrochemical performance	Reference
KMnF-LE	138 mAh g⁻¹ for 100 cycles at 50 mA g⁻¹, 110 mAh g⁻¹ for 10000 cycles at 400 mA g⁻¹	This work
a-Ti ₃ C ₂	98 mAh g ⁻¹ for 20 cycles at 20 mA g ⁻¹ , 42 mAh g ⁻¹ for 500 cycles at 200 mA g ⁻¹	Ref 6
Ti ₃ C ₂	46 mAh g ⁻¹ for 100 cycles at 20 mA g ⁻¹	Ref 7
M-KTO	119 mAh g ⁻¹ for 12 cycles at 50 mA g ⁻¹ 47 mAh g ⁻¹ for 900 cycles at 200 mA g ⁻¹	Ref 8
Sn foil	66 mAh g ⁻¹ for 300 cycles at 50 mA g ⁻¹	Ref 9
Graphite	100 mAh g ⁻¹ for 50 cycles at 140 mA g ⁻¹	Ref 10
Soft carbon	185 mAh g ⁻¹ for 50 cycles at 558 mA g ⁻¹	Ref 10
Hard carbon	216 mAh g ⁻¹ for 100 cycles at 27.9 mA g ⁻¹	Ref 11
K ₂ Ti ₈ O ₁₇ nanorod	110.7 mAh g ⁻¹ after 50 cycles at 20 mA g ⁻¹	Ref 12
Bulk K ₂ Ti ₈ O ₁₇	50 mAh g ⁻¹ after 50 cycles at 20 mA g ⁻¹	Ref 12
Carbon Nanofibers	80 mAh g ⁻¹ after 20 cycles at 50 mA g ⁻¹	Ref 13
RGO films	120 mAh g ⁻¹ after 100 cycles at 10 mA g ⁻¹	Ref 14
KTi ₂ (PO ₄) ₃	36 mAh g ⁻¹ after 100 cycles at 64 mA g ⁻¹	Ref 15
KTi ₂ (PO ₄) ₃ /C	82 mAh g ⁻¹ after 100 cycles at 64 mA g ⁻¹	Ref 15
K ₂ PC	158 mAh g ⁻¹ after 100 cycles at 44 mA g ⁻¹	Ref 16
polynanocrystalline graphite	80 mAh g ⁻¹ after 300 cycles at 100 mA g ⁻¹	Ref 17

Energy & Environmental Science

Table S4. The energy and volume change before and after K intercalation of different KMF. Comparison of volume (in Å³/cell) of pristine KMnF₃ (K₈Mn₈F₂₄), one K intercalated pristine KMnF₃ (K₉Mn₈F₂₄), KMnF₃ with vacancies (K₅Mn₈F₂₁), three K intercalated KMnF₃ with vacancies (K₈Mn₈F₂₁), four K intercalated KMnF₃ with vacancies (K₉Mn₈F₂₁) and six K intercalated KMnF₃ with vacancies (K₁₁Mn₈F₂₁), and K insertion energy (in eV) of K₉Mn₈F₂₄ (compared to K₈Mn₈F₂₄), K₈Mn₈F₂₁ (compared to K₅Mn₈F₂₁) and K₉Mn₈F₂₁ (compared to K₉Mn₈F₂₁).

	K ₈ Mn ₈ F ₂₄	K ₉ Mn ₈ F ₂₄	K ₅ Mn ₈ F ₂₁	K ₈ Mn ₈ F ₂₁	K ₉ Mn ₈ F ₂₁	K ₁₁ Mn ₈ F ₂₁
Energy	-	1.1	-	-1.21	0.52	0.725
Volume	614.352	655.537	599.357	607.537	623.744	729.100

Supplementary References

1. D. W. Su, A. McDonagh, S. Z. Qiao and G. X. Wang, *Adv. Mater.*, 2017, **29**, 1604007.
2. J. Y. Wang, H. J. Tang, L. J. Zhang, H. Ren, R. B. Yu, Q. Jin, J. Qi, D. Mao, M. Yang, Y. Wang, P. Liu, Y. Zhang, Y. R. Wen, L. Gu, G. H. Ma, Z. G. Su, Z. Y. Tang, H. J. Zhao and D. Wang, *Nature Energy*, 2016, **1**, 16050.
3. C. Yang, S. Yu, C. F. Lin, F. Lv, S. Q. Wu, Y. Yang, W. Wang, Z. Z. Zhu, J. B. Li, N. Wang and S. J. Guo, *ACS Nano*, 2017, **11**, 4217-4224.
4. T. Brezesinski, J. Wang, S. H. Tolbert and B. Dunn, *Nat. Mater.*, 2010, **9**, 146.
5. D. Chao, C. Zhu, P. Yang, X. Xia, J. Liu, J. Wang, X. Fan, S. V. Savilov, J. Lin, H. J. Fan and Z. X. Shen, *Nat. Commun.*, 2016, **7**, 12122.
6. P. C. Lian, Y. F. Dong, Z. S. Wu, S. H. Zheng, X. H. Wang, S. Wang, C. L. Sun, J. Q. Qin, X. Y. Shi and X. H. Bao, *Nano Energy*, 2017, **40**, 1-8.
7. Y. Xie, Y. D. Agnese, M. Naguib, Y. Gogotsi, M.W. Barsoum, H. L. Zhuang and P. R. C. Kent, *ACS Nano*, 2014, **8**, 9606-9615.
8. Y. F. Dong, Z. S. Wu, S. H. Zheng, X. H. Wang, J. Q. Qin, S. Wang, X. Y. Shi and X. H. Bao, *ACS Nano*, 2017, **11**, 4792-4800.
9. B. F. Ji, F. Zhang, X. H. Song and Y. B. Tang, *Adv. Mater.*, 2017, **29**, 1700519.
10. Z. L. Jian, W. Luo and X. L. Ji, *J. Am. Chem. Soc.*, 2015, **137**, 11566-11569.
11. Z. L. Jian, Z. Y. Xing, C. Bommier, Z. F. Li and X. L. Ji, *Adv. Energy Mater.*, 2016, **6**, 1501874.
12. J. Han, M. W. Xu, Y. B. Niu, G. N. Li, M. Q. Wang, Y. Zhang, M. Jia and C. M. Li, *Chem. Commun.*, 2016, **52**, 11274-11276.
13. W. Luo, J. Y. Wan, B. Ozdemir, W. Z. Bao, Y. N. Chen, J. Q. Dai, H. Lin, Y. Xu, F. Gu, V. Barone and L. B. Hu, *Nano Lett.*, 2015, **15**, 7671-7677.
14. Y. Liu, F. F. Fan, J. W. Wang, Y. Liu, H. L. Chen, K. L. Jungjohann, Y. H. Xu, Y. J. Zhu, D. Bigio, T. Zhu and C. S. Wang, *Nano Lett.*, 2014, **14**, 3445-3452.
15. J. Han, Y. B. Niu, S. J. Bao, Y. N. Yu, S. Y. Lu and M. W. Xu, *Chem. Commun.*, 2016, **52**, 11661-11664.
16. Q. J. Deng, J. F. Pei, C. Fan, J. Ma, B. Cao, C. Li, Y. D. Jin, L. P. Wang and J. Z. Li, *Nano Energy*, 2017, **33**, 350-355.
17. Z. Y. Xing, Y. T. Qi, Z. L. Jian and X. L. Ji, *ACS Appl. Mater. Inter.*, 2016, **9**, 4343-4351.